In-line characterisation of continuous phase conductivity in slurry flows using artificial intelligence tomography

Machin, Thomas D.; Wei, Kent; Greenwood, Richard W.; Simmons, Mark J.h.

DOI:
10.1016/j.mineng.2021.107203

Document Version
Peer reviewed version

Citation for published version (Harvard):
Machin, TD, Wei, K, Greenwood, RW & Simmons, MJH 2021, 'In-line characterisation of continuous phase conductivity in slurry flows using artificial intelligence tomography', *Minerals Engineering*, vol. 173, 107203. https://doi.org/10.1016/j.mineng.2021.107203

In-line Characterisation of Continuous Phase Conductivity in Slurry Flows using Artificial Intelligence Tomography

Thomas D. Machin[a,c], Kent Wei[b], Richard W. Greenwood[a], Mark J. H. Simmons[a]

[a] School of Chemical Engineering, University of Birmingham, Edgbaston, B15 2TT
[b] Industrial Tomography Systems Ltd, Manchester, M3 3JZ
[c] Stream Sensing Ltd, Manchester, M3 3JZ

Abstract

Electrical Impedance Tomography (EIT) can be applied to monitor a variety of mineral and chemical processes including: velocity measurements in drilling cuttings and hydrocyclone operations. Hydraulic conveying systems rely upon the knowledge of slurry density to ensure efficient transportation of the solids. Typically, density measurements exploit the attenuation of gamma ray photons which poses complex safety, operational and regulatory concerns with Electrical Impedance Tomography affording a non-nuclear alternative to traditional approaches. To optimise the accuracy of this non-nuclear density measurement, the electrical conductivity of the aqueous phase in a multi-component slurry, is required. Whilst conductivity probes are sufficiently accurate, there are often drawbacks and limitations due to installation restrictions, as it is difficult to separate aqueous and solid phases in real-time. Electrical Impedance Fingerprinting (EIF), is a novel measurement technique which characterises formulation properties, in-situ, based upon electrical impedance sensing and artificial intelligence algorithms. This paper outlines the development of EIF and its application to monitor aqueous phase conductivity in multi-component slurries, containing sands and clays. EIF accurately predicts this conductivity with high accuracy and a root-mean squared error of 0.055 mS cm^{-1}. This development ensures accurate non-nuclear density measurements (< 5%) are obtained across an extended aqueous electrical conductivity range of 1.5 – 70 mS cm^{-1}. This encompasses the majority of target hydraulic conveying systems in mining operations. EIF also enhances the functionality of 'traditional' electrical tomography as not only are mineral processes able to be visualised, but the process materials are simultaneously characterised, to improve process understanding, optimisation and control.

1. Introduction

Hydraulic conveying systems often rely upon the knowledge of slurry density and flow parameters for the optimisation of their performance. These parameters ensure that sufficient mobile solids are being conveyed, pipeline blockage has not occurred and production targets are being achieved (Williams and Vilar, 2008). Such continuous slurry density measurements typically exploit the attenuation of gamma ray photons; however, the use of nuclear sources poses complex safety, operational, and regulatory concerns (Batey, 2012). These arise throughout the entire instrument lifetime from initial transport to disposal of the radioactive waste with significant being costs incurred. Thus, there is a strong commercial demand to develop a non-nuclear alternative to the density measurement with studies being conducted using various sensing media, including: ultrasound, microwave and Coriolis meters (Wei et al., 2016). Despite such attempts, these techniques were found to be unsuitable for applications in industrial pipelines due to material abrasiveness, process requirements and pipe diameter restrictions (Batey, 2012). Electrical Impedance Tomography (EIT) provides a robust in-line, non-nuclear alternative for this density measurement (Wei et al., 2016). In minerals engineering, there are many additional applications requiring solids to be monitored in slurry flows (Scott and McCann,

2005; Fangary and El Ghani, 1997; Cullivan et al, 2003). In addition to monitoring the transport of particle-bearing fluids (Wang et al, 2003), EIT has been applied to velocity measurements in clay-based drilling muds, monitoring of hydrocyclone separation for minerals (Cullivan et al, 2004; Nowakowski et al, 2004), and water and oil/water separations (Bennett and Williams, 2004; Williams et al, 1999).

A tomographic measurement requires the acquisition of signals from sensors located around the periphery of the subject domain i.e., a pipe or a vessel (Williams and Beck, 1995). Such signals are then able to uncover information about the nature and distribution of components that are located within the sensing domain (Dyakowski and Jaworski, 2003). To attain such information, a vast number of tomographic modalities exist which exploit differing sensing media, including: acoustic tomography (Kohn, 1995); X-ray computed tomography (Kalender, 2006) and optical tomography (Zimnyakov and Tuchin, 2002). Electrical Tomography techniques afford an imaging solution which is non-invasive, safe, dynamic and low cost and hence has extensively been employed within industrial applications to analyse production (York, 2001). There are three common types of Electrical Tomography modalities, EIT, Electrical Capacitance Tomography (ECT) and Electrical Resistance Tomography (ERT), which obtain the distribution of impedance, capacitance and resistance, respectively, within a subject domain.

EIT obtains the electrical impedance distribution by applying alternating currents or voltages to the domain, according to a pre-defined measurement protocol (Wang, 2015); the response signals are subsequently captured by the remaining electrodes. These signals are then reconstructed, using an algorithm, into an image of the cross-sectional impedance distribution in the sensing domain (Soleimani, 2005). These raw tomography measurements are able to provide information about the following characteristic electrical properties of the interrogated media: resistance, reactance, phase shift and impedance.

Effective media approximations are then utilised to convert the electrical impedance distribution of macroscopically inhomogeneous media into the volumetric concentration of solids (Markel, 2016). Typical effective media approximations include the Maxwell-Garnett and Bruggeman equations, highlighted in Eqs (1) and (2), respectively below. It must be noted, that these equations are only applicable to a single mineralic phase systems with multi-mineralic systems requiring more complex analyses. When such analyses are required the measurement of aqueous phase conductivity is necessary to obtain accurate slurry density measurements.

$$\alpha = \frac{2\sigma_c + \sigma_d - 2\sigma_m - \left(\frac{\sigma_m \sigma_d}{\sigma_c}\right)}{\sigma_m - \left(\frac{\sigma_d \sigma_m}{\sigma_c}\right) + 2(\sigma_c - \sigma_d)} \tag{1}$$

where α is the dispersed phase volume fraction, and σ_c, σ_d and σ_m are the continuous (liquid) phase, dispersed (solid) phase and slurry conductivities, respectively.

$$\alpha = 1 - \left(\frac{\sigma_m - \sigma_d}{\sigma_c - \sigma_d}\right)^3 \sqrt{\frac{\sigma_c}{\sigma_m}} \tag{2}$$

Upon obtaining the volumetric concentration distribution from the above equations, it is averaged and then converted to density using a mass balance; the density of the solids must already be known. This non-nucleonic technique has been validated in a number of operational hydraulic conveying installations (McCormack et al., 2016; Wei et al., 2018).

Effective media approximations, such as (1) and (2), rely upon the knowledge of the electrical conductivity of the aqueous fluid to produce accurate density measurements. This information is also vital for the optimisation of the non-nucleonic density technology to select appropriate analysis algorithms and improve the information gained from the raw data.

Whilst a conductivity probe is sufficiently accurate and are typically fitted into hydraulic conveying installations where EIT is present (McCormack et al., 2016; Wei, et al., 2018), there are a number of drawbacks. To function appropriately for EIT, a conductivity probe is required to be submersed into the aqueous fluid without the solids being present; this is often unlikely during processing. Often, probes must be installed away from the EIT sensing location, with the conductivity of the aqueous fluid obtained from elsewhere in the process, not reflective of the material measured by the EIT sensor. Thus an integrated approach is highly desirable.

To overcome this challenge, a novel measurement technology, Electrical Impedance Fingerprinting (EIF), has been developed which is able to fingerprint and identify a fluid within the pipe, by combining raw tomographic data and artificial intelligence algorithms. Whilst traditional image reconstruction approaches, allow the visualisation of the distribution of materials within the sensing domain, information gathered from the raw response signals may also contain intrinsic links to vital process parameters. This direct relation, via artificial intelligence, is often of greater interest than their estimation from reconstructed tomographic images (Mohammed-Saleh and Hoyle, 2002). Aligned with the emergence of digital manufacturing, artificial intelligence algorithms are increasingly being applied to tomographic measurements, to develop appropriate, novel, in-line sensing and diagnostic methods (Hartman et al., 2019). Machine learning algorithms have been effectively applied to ECT to monitor: component fractions in multiphase oil-water-air flows (Mohamad-Saleh and Hoyle, 2002), flow regime prediction in water-air systems (Johansen et al., 2018) and interface detection of oil-based systems within horizontal pipes (Ru et al., 2011). ECT measurements used in such studies are limited to dielectric materials and the outputted results are unsuitable for large diameter sensors and aqueous systems, such as those observed in hydraulic conveying operations. ECT may be applied when the fluid is a non-conducting solvent.

EIF utilises the phase information obtained from non-invasive micro-electrical tomography sensors, coupled with artificial intelligence, to provide real-time identification of fluids within a pipe. EIF may be utilised across a wider range of process applications and fluids for example real-time, formulation characterisation such as the evolution of mixing in an agitated vessel, or froth flotation tank. Once recognised, the fluid fingerprint can then be directly related to a number of the aforementioned key quality and structural attributes for example rheological properties and product composition. The focus of this paper is the application of EIF to in-line conductivity measurements for use in non-nuclear densitometry.

This paper presents the application of EIF to hydraulic conveying systems for extraction of the aqueous phase conductivity in multi-component slurries; the underlying principles of this technique are also outlined alongside experimental measurements to demonstrate its suitability. The aqueous conductivity has been monitored within a range of multi-component slurries consisting of kaolin and sand, across a range of solid concentrations and flow regimes, to demonstrate that EIF is a powerful characterisation tool.

2. Development of Electrical Impedance Fingerprinting

2.1 The ‘Fingerprint’

To obtain impedance properties, EIT, measures the change in amplitude of sinusoidal response signals and their phase shift. For a fixed sinusoidal frequency, the circular adjacent-electrode EIT measurement protocol for a 16 electrode sensor provides 104 individual phase measurements (Wang, 2015); these measurements are used as an electrical fingerprint of a formulation, or process. In fluids of low admittivity, this fingerprint remains uniform, with a repeatable parabolic shape witnessed for a tomography measurement cycle. In the first measurement cycle, the input signal is applied to a single pair of electrodes, with the response signals measured by the remaining electrode pairs. This approach is then repeated for subsequent electrode pairs with the input signal being moved to successive electrode pairs. The measurement approach for EIT and EIF is highlighted in Figure 1.

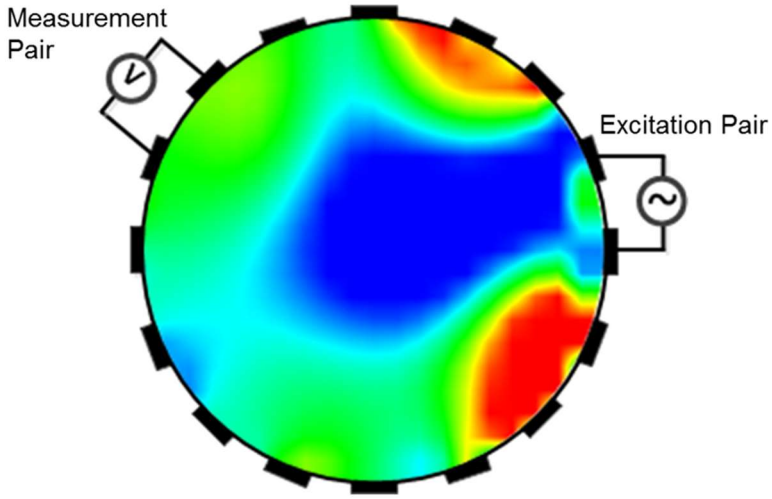

Figure 1 EIT and EIF sensing configuration and tomogram

As the admittivity of the fluid is increased, the structure of the fingerprint becomes progressively disordered until the measurement cycles are no longer discernible. To accentuate such shape effects and obtain the fingerprint, the phase measurements are normalised across each measurement cycle; this behaviour is the foundation of EIF.

Example fingerprints are illustrated in Figures 2a and 2b; these fingerprints represent water of electrical conductivity adjusted to 0.1 mS cm^{-1} and 20 mS cm^{-1}, respectively, via the addition of sodium chloride. This conductivity was measured using a HANNA conductivity probe at room temperature. These fingerprints were obtained from a circular 16-electrode EIT sensor, of diameter 25.4 mm, supplied by Industrial Tomography Systems Ltd (ITS). This sensor was connected to the p2+ EIT data acquisition system, also supplied by ITS, with the measurement acquired at a fixed injection current frequency of 19.2 kHz.

As the phase measurement does not require reconstruction to be performed, nor is it based upon a reference, this technique is advantageous over traditional tomography as it is directly related to absolute process properties.

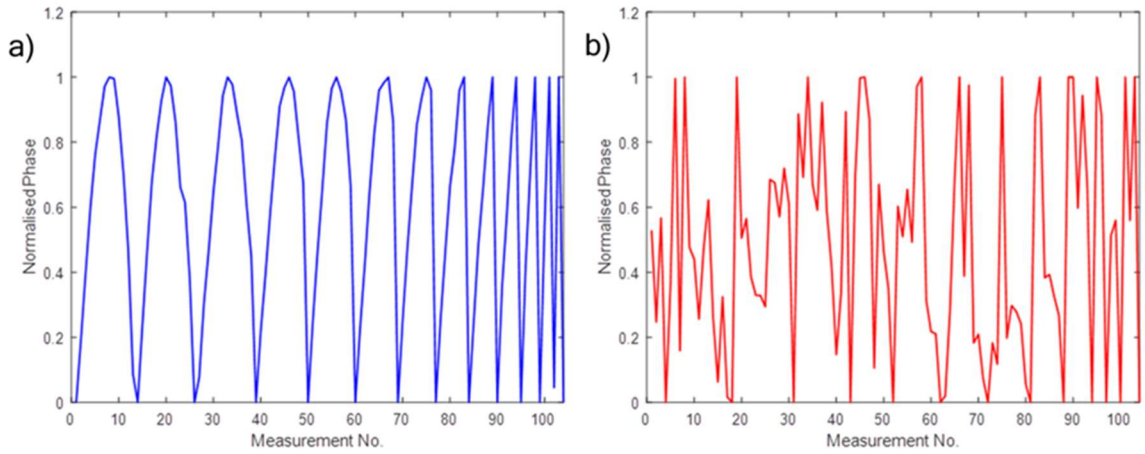

Figure 2 Electrical Impedance Fingerprint– p2+ EIT Instrument: a) 0.1 mS cm^{-1}; b) 20 mS cm^{-1}

Jiang and Soleimani (2018), performed a series of computational experiments to simulate the wideband phase measurements in an EIT sensor filled with a 1 mS cm^{-1} fluid. These results were validated, experimentally, by measuring the phase with an Electrical Impedance analyser. In both cases, similar shapes to Figure 2a, were observed providing initial confidence in the measurement. It must be noted that the frequency of the sinusoidal input signal was 500 kHz.

To provide further validation and to ensure that the pattern obtained was not a function of the instruments electronics, but is tracking changes in formulation, an independent EIT instrument was utilised. The secondary system, z8000 EIT data acquisition instrument, supplied by ITS, possesses a different data acquisition protocol. A comparison of specification of the two instruments is highlighted in Table 1. It must also be noted that the z8000 system is no longer commercially available and hence the ITS p2+ system is used throughout the remainder of the paper.

Table 1 Electrical Tomography modality system parameters (ITS, 2020)

Instrument	**z8000**	**p2+**
Parameter	Impedance	Impedance
Excitation Source	Current	Current
Response Signal	Voltage	Voltage
Excitation Frequency (kHz)	10, 20, 40, 80	0.0075 – 153.6
Temporal Resolution (fps)	100	3
Measurement Accuracy	± 0.5 %	± 0.5 %
Sensitivity (µV)	4.88	4.88
Spatial Resolution	5 %	3 - 5 %
Fluid Conductivity (mS cm^{-1})	0.1 - 70	0.1 – 70
Phase Measurement Protocol	Phase Sensitive Demodulation	Phase Sensitive Demodulation
Demodulation Technique	4 - point	2 - point
Phase Sampling	8, each electrode	1, adjacent pairs

The z8000 instrument was connected to the same sensor used previously. The Electrical Impedance Fingerprint was then obtained with water of electrical conductivity set to 0.5, 1, 5 and 10 mS cm^{-1}, for Figures 3a, 3b, 3c and 3d, respectively. This conductivity was also adjusted via the addition of sodium chloride.

Once again, in relatively low conductivity media, 0.5 mS cm^{-1}, a uniform fingerprint is observed with each measurement cycle being discernible. However, as the admittivity is increased, Figure 3d, the fingerprint repeatedly begins to break down. As the independent EIT modalities exhibit similar behaviour, it can be postulated that this alteration in phase behaviour is universal across electrical impedance tomography modalities and cannot be solely attributed to the ITS p2+ instrument. This increases the reliability, in-plant and on-site applicability and robustness of EIF.

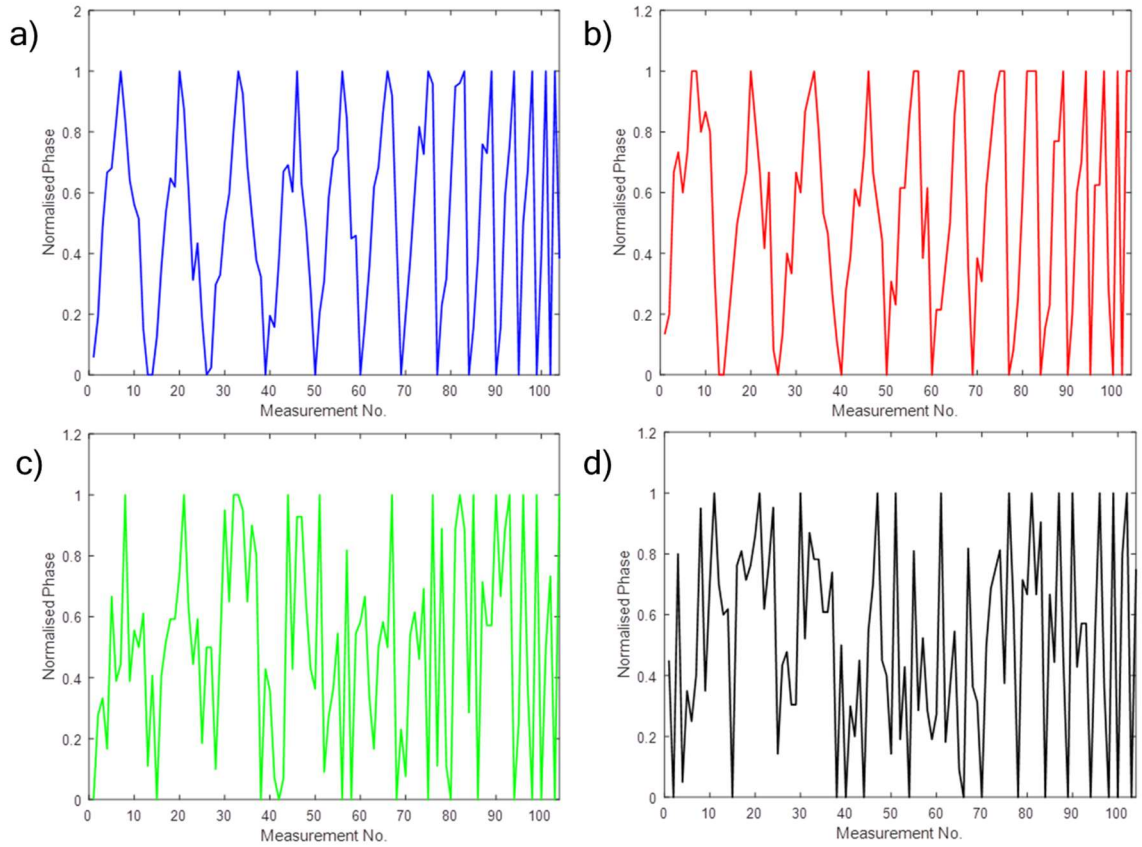

Figure 3 Electrical Impedance Fingerprint – z8000 EIT Instrument: a) 0.5 mS cm^{-1}; b) 1 mS cm^{-1}; c) 5 mS cm^{-1}; d) 10 mS cm^{-1}

The Electrical Impedance Fingerprint and traditional tomographic data are captured simultaneously and using the same interrogating electrodes; this enables the process to be visualised as well as the formulation characterised.

The quality of the tomographic data is often dependent upon the current signal generator settings. Consequently, the impact of the alternating current signal generator upon the fingerprint was also investigated by varying the following tomography input parameters: current source, current magnitude, sample cycles and programmable gain amplifier settings (gain map).

Using initial p2+ data acquisition settings of a 15 mA injection current from the current source rated 1.5 – 15 mA, 20 sample cycle delays and 19.2 kHz frequency, 100 impedance fingerprints were captured for water of conductivity 1 mS cm^{-1}. Each of the 104 normalised phase measurements, which form the fingerprint, were averaged across the 100 measurements. These were then compared to measurements obtained when the signal generator settings are altered. The individual normalised phase measurements are depicted in Figure 4, in the form of a parity plot. The 'normalised phase', is obtained from normalising the captured phase measurements across each tomography measurement

cycle. For each measurement cycle, a single pair of electrodes are used for injection, with the remaining electrodes used for measurement. In the next measurement cycle, the injection electrodes pair is then changed. This normalisation ensures that the shape of the fingerprint is emphasised and not the magnitude.

Performing a linear regression of all 104 phase measurements yielded correlation coefficients of 0.997, 0.998, 0.999 and 0.993 when the current source, current magnitude, sample delay cycles and gain are changed, respectively. This indicates the parameters of the signal generator have little impact upon the shape of the phase measurement. The p-values for this fitting were also found to be below 0.001, indicating a high level of statistical significance between the fingerprints.

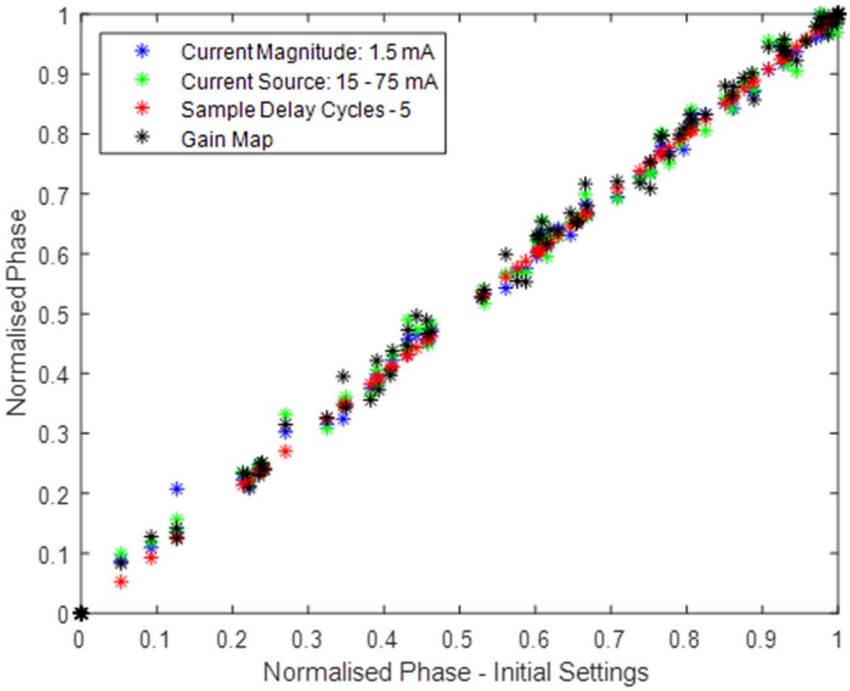

Figure 4 The impact of signal generator settings upon the Electrical Impedance Fingerprint

As a result, the optimal tomography settings are able to implemented with little variation in the fingerprint observed. This ensures that both 'traditional' tomography analyses and EIF can be performed simultaneously without detriment to either approaches. This enhances the capability of EIT to not only to visualise the spatial distribution of materials within the sensing domain, but to also simultaneously be able to identify the fluid or formulation present. This method can thus be applied as a tool for greater process understanding, optimisation and control.

The removal of the reference further enhances the potency of EIF as process information is directly obtained without the requirement of estimation from a reconstructed image. This was highlighted in a study by Stephenson (2008) who demonstrated that a tomogram reconstructed using the linear back projection algorithm can give rise to an image error for central and edge conclusions of 16.1 % and 27.9 %, respectively.

2.2 Artificial Intelligence

Upon obtaining the electrical fingerprint, supervised artificial intelligence (AI) techniques may be employed to extract further valuable process information. Based upon *a priori* knowledge, AI algorithms are trained to recognise the features of the fingerprint and develop models from experience of independent experimental data. The developed fingerprint models are flexible and are able to monitor a wide range of key quality attributes such as electrical conductivity, formulation properties and flow regimes. Such techniques are increasingly of interest to industry for process analytics and control enabling predictive models to be developed adaptively (Bernardes and Costelo-Branco, 2017). For both classification and characterisation problems, 'traditional' machine learning algorithms and artificial neural networks have been explored for the optimisation of EIF.

Using an initial trial and error approach, a variety of training algorithms were investigated including: support vector machines, decision trees, nearest neighbour classifiers and discriminant analyses.

It was found that Artificial Neural Networks (ANNs) provided the best performance when utilising the Electrical Fingerprint to extract process information, based upon the criteria of adaptability and accuracy. ANNs are powerful prediction tools which consist of an interconnected assembly of elements, known as neurons, with functionality similar to an animal neuron (Gurney, 1997). Such systems extract linear combinations of measurement inputs and then model the target data as a non-linear function, forming an extremely powerful forecasting tool (Hastie et al., 2008). With differences in the fingerprint visible by eye, the required network architecture remained relatively simple without the requirement for deep learning approaches. Consequently, for both classification and continuous prediction scenarios, two-layer feedforward neural network architectures were investigated (Agarwal, 2018). The neural network architecture employed in this study for continuous predictions is depicted in Figure 5.

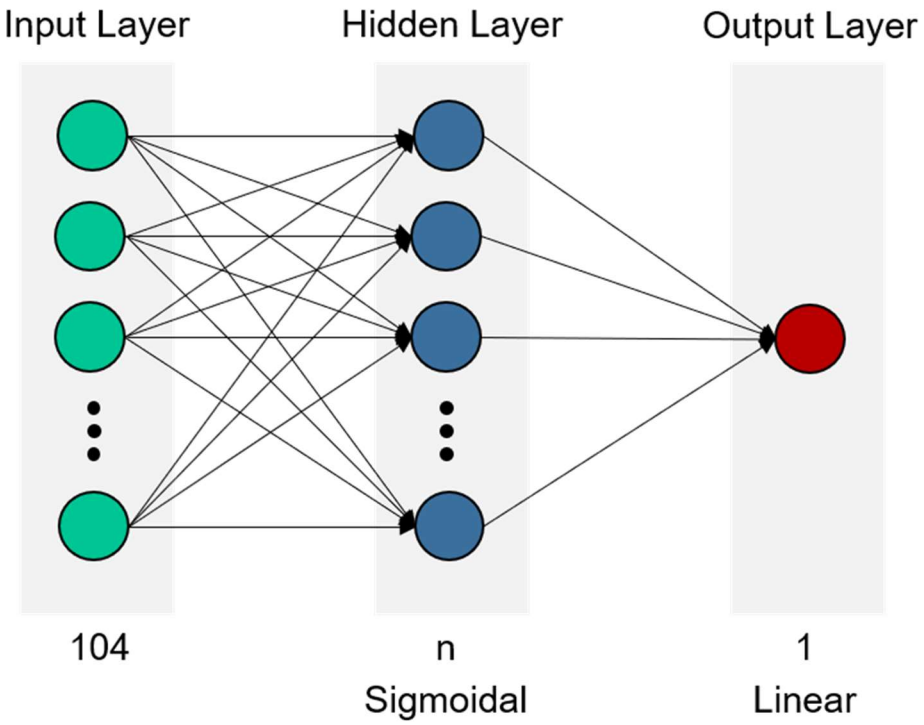

Figure 5 Optimised ANN architecture for predictions of continuous variables

A logistic sigmoidal transfer function was selected in the hidden layer, as it provides improved results when compared to the conventional step activation function (Gurney, 1997). This transfer function is

also extremely common within multi-layer neural networks (Rashid, 2016). In continuous problems, the output layer consists of a single neuron and a linear transfer function.

3. Methodology

3.1 Materials

Characterisation experiments were performed to explore the application of EIF to monitor the continuous phase electrical conductivity in multi-component slurries. Within aqueous-based hydraulic transport applications, the aqueous phase properties are known to vary both in conductivity and pH, within the ranges of 0.1 - 70 mS cm^{-1} and 5.5 – 8.5, respectively (Wright and Colling, 1995). However, in EIT densitometry measurements, the importance of the aqueous conductivity measurement is diminished for values in excess of 30 mS cm^{-1}, and thus the conductivity range was reduced to 0.1 – 30 mS cm^{-1}.

To create the aqueous phases, ammonium acetate (Sigma-Aldrich, UK) was utilised to adjust the conductivity of de-ionised water (Hexal Chemicals Ltd, UK). Ammonium acetate was selected as it alters the ionic concentration without changing the pH and the acetate co-ions at the particle-particle interface prevent competition between negatively charged ions. Moreover, the ions are univalent, as in sodium chloride, the most common electrolyte found in hydraulic transport applications (Wright and Colling, 1995). The pH was adjusted via the addition of either sodium hydroxide or glacial acetic acid (Sigma-Aldrich, UK), to reduce and increase the pH, respectively. To ensure that the finalised conductivity and pH were as desired, handheld conductivity and pH probes were utilised (HANNA Instruments, UK). These aqueous phase parameters were measured prior to solids being added, to formulate the slurries. This conductivity was used in the training of the EIF technology, to predict aqueous phase conductivity of multi-component slurries.

Varying concentrations of Kaolin SUPREME^{TM} (Imerys UK), were added to these aqueous solutions to formulate the experimental clay slurries. This kaolin was selected due to ultrafine average particle size, of 0.4 µm, its high surface area (Imerys, 2018) which maximises the contribution of the clay's surface contributions.

Sand was soaked in de-ionised water for 24 hours to remove precipitated electrolytes and subsequently added to the aqueous solutions to form either sand or multi-component slurries. A Taguchi design of experiments was employed to orthogonally alias the impacting factors with the finalised design parameters displayed in Table 2 (Jones and Goos, 2011).

Table 2 Experimental Parameters

Slurry Parameter	Experimental Values
Aqueous Conductivity (mS cm^{-1})	0.15 - 30
Dispersed Phase Concentration (wt%)	0, 5, 10, 20, 25, 30
Dispersed Phase Composition (wt%)	0, 20, 25, 33, 50, 100 (both kaolin and sand)
pH	5.5, 7, 8.5

3.2 Experimental Setup

Measurements were performed using a two-plane, 25.4 mm diameter EIT sensor, under both agitated and pipe flow conditions. In the former, end caps were attached to the flanges of the sensor at one end with the test materials added; this consisted of 70 mL aliquots of the aqueous phase solutions

and solids in their specified concentrations. This sensor was aligned vertically, to reduce the number flow regimes present, with the solids suspended using a magnetic stirrer at a fixed rotational speed. Due to the small particle size, kaolin was easily suspended; however, to ensure the effective suspension of sand and sand-kaolin mixtures, the "just-suspended" criterion was observed.

Pipeline experiments were additionally performed within a simple recirculating flow loop, in which a 7.5 L acrylic vessel, *T = 21 cm*, a peristaltic pump, supplied by Watson-Marlow, UK, and the EIT sensor were connected in series. Upon loading into the vessel, a four-blade down-pumping pitched blade turbine, *D = 0.3T, C = 0.3T,* was utilised to disperse the solids within the vessel. The Zweitering just-suspended impeller speed, N_{js}, (Zweitering, 1958) was calculated for this setup, using (3), and implemented with the criterion visualised to validate this (Ayranci and Kresta, 2014).

$$N_{js} = S\left(\frac{g(\rho_d - \rho_c)}{\rho_c}\right)^{0.45} {d_p}^{0.2} X^{0.13} \left(\frac{\rho_d}{\mu_c}\right)^{0.1} D^{-0.85} \tag{3}$$

where S is a Zwietering constant, g is the acceleration due to gravity, 9.81 m s^{-2}, ρ_c and ρ_d are the continuous phase densities, in kg m^{-3}, respectively, d_p is mean particle size diameter, in m and μ_c is the continuous phase viscosity, in Pa s.

The suspended slurries are then circulated with the EIT sensor oriented vertically to minimise the number of flow regimes present, increase dispersion and reflect the operating conditions in which traditional nuclear density meters are installed (Golgoun et al, 2016). Once steady state had been reached, the aforementioned EIT measurements were performed for each experimental condition. Some experiments were also conducted with the EIT sensor oriented horizontally, to assess the performance of the technique in bed flows.

3.3 Electrical Impedance Tomography

A dual-plane, 16-electrode EIT sensor, of diameter 25.4 mm, was utilised within this study. The body of the EIT sensor was manufactured in clear acrylic, this allowed the solids distribution and flow regimes within the sensor to be visualised. The EIT sensor was connected to the ITS p2+ EIT instrument, supplied by ITS, with the circular complex adjacent measurement protocol selected with partial gain. The excitation signal in each case was fixed to 15 mA and the current source, 1.5 – 15 mA, was selected to act as a compromise between the current source purity and to maximise the magnitude of outputted voltages based upon knowledge of the aqueous phase ionic concentration. The capture of appropriate response voltages ensure that the integrity of the reconstructed tomographic data is preserved. A frequency optimisation step was additionally performed prior to testing with the optimal operating current injection frequency range observed to be between 2.4 and 19.2 kHz for the ITS p2+ instrument. The latter frequency was selected for all EIT experiments due to its increased stability to complex measurements.

For each experimental condition described in Table 2, 250 frames were captured to ensure repeatability of the real and imaginary voltage measurements. The prevention of class imbalance eliminates the requirement to use more complex predictors such as RUSBoost, AdaBoost and SMOTEBoost (Seiffert et al., 2010; Freund, 2006; Chawla et al., 2003).

The ITS p2+ software was utilised to extract the raw voltage measurements which were then subsequently imported into MATLAB. The Electrical Impedance Fingerprints then computed before being randomly segmented into training, validation and test data, which equate to 70 %, 15 % and 15 % of the entire dataset, respectively. The training dataset consists of 34,300 electrical impedance fingerprint measurements which encompass 90 slurry compositions whose discrete phases consist of

kaolin, sand, or both. Of these systems, the largest inclusion of solids equated to 28 vol% with the operational range of EIT densitometry, 0 – 35 vol%, and thus these datasets provide a comprehensive analysis of any developed algorithms. This data was then fed into the MATLAB Deep Learning Toolbox utilised to train the appropriate Artificial Neural Networks.

4. Results

4.1 Impact of solids upon the Electrical Impedance Fingerprint

An understanding of the in-line aqueous phase conductivity is vital in the optimisation of the EIT non-nuclear density measurements for appropriate analysis algorithm selection and voltage compensation. Hence, this application of Electrical Impedance Fingerprinting to multi-phase slurries was examined, for dispersed flows.

The shape of the phase measurements, the fingerprint, appears to be independent of solids addition in dispersed phase flows; it is acknowledged that the magnitude of the phase measurement varies during the addition of solids. This approach is valuable in a number of applications such as monitoring the aqueous phase to optimise non-nuclear density measurements in hydraulic conveying systems or the progress of a multi-phase reaction. To validate this, the fingerprint is examined at a fixed aqueous phase conductivity, of 0.15 mS cm^{-1}, with the kaolin content then varied from 0 – 20 wt%. A parity plot, Figure 6, is used to demonstrate the independence of the 104 fingerprint measurements to solids content.

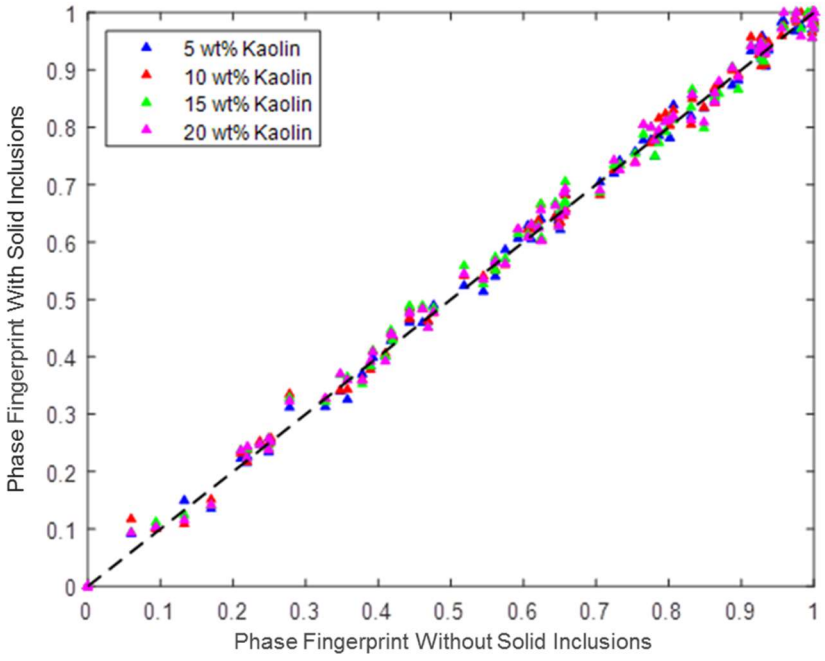

Figure 6 A parity plot demonstrating the impact of kaolin addition upon the Electrical Impedance Fingerprint

A linear relationship is observed between the individual measurements of the fingerprint when solids are present and when they are not; this is highlighted by a highly negative Akaike Information Criterion (AIC) of -465.6 for a linear fitting. Consequently, a linear regression of the phase measurements with and without solids, yielded high correlation coefficients of 0.9982, 0.9975, 0.9970 and 0.9973 for 5,

10, 15 and 20 wt% kaolin additions, respectively. In each instance the p-values for the fitting were seen to be less than 0.001, demonstrating that the variables observed a high level of statistically significance. Alongside such linearity, the gradient of the aforementioned fittings were on average 1.000 indicating the magnitude of the measured variables is identical.

This demonstrates that the Electrical Impedance Fingerprint is independent of solids content, in dispersed flows, and highlights the potential of EIF to be employed as in-line measurement of continuous phase electrical conductivity in multiphase slurry flows.

4.2 Artificial Neural Network Optimisation

To investigate this potential and optimise the performance of this approach, the two-layer feedforward neural network architecture (TLFNN), presented in Figure 5, is investigated. A number of algorithms are available to train the weights and biases of the selected neural network, namely: Scaled-Conjugate Gradients (SCG), Levenberg-Marquadt (LM) and Bayesian Regularisation. When applying both the SCG and LM training algorithms six validation checks were performed to ensure that the algorithm had reached a global minimum.

Whilst unsuitable for classification problems, the Levenberg-Marquadt (LM) algorithm offers advantages when analysing continuous problems. This algorithm has been extensively used within electrical tomography as a reconstruction algorithm (Tan et al., 2011) and for a parametric fitting in a novel in-line rheometer, based upon electrical resistance sensing (Machin et al., 2018). Bayesian regularisation and scaled conjugate gradient approaches have also been explored as potential training algorithms (Neal, 1996).

The continuous TLFNN architecture was trained using each of the aforementioned algorithms, using all of the experimental data collected, approximately 48,000 data frames; this dataset was randomly segregated into 70 % training, 15 % validation and 15 % test data. For each condition, the algorithm was trained five times, with the Mean Squared Error (MSE) of the test dataset and training time, averaged and captured to assess accuracy and adaptiveness, respectively. The accuracy of the measurement compares the aqueous phase conductivity captured in the multiphase slurries using EIF to that measured by the conductivity probe, prior to the solids being added. This analysis was also repeated to optimise the number of neurons in the hidden layer, with this being varied from 10 – 70 neurons. A summary of this analysis is depicted in Figure 7.

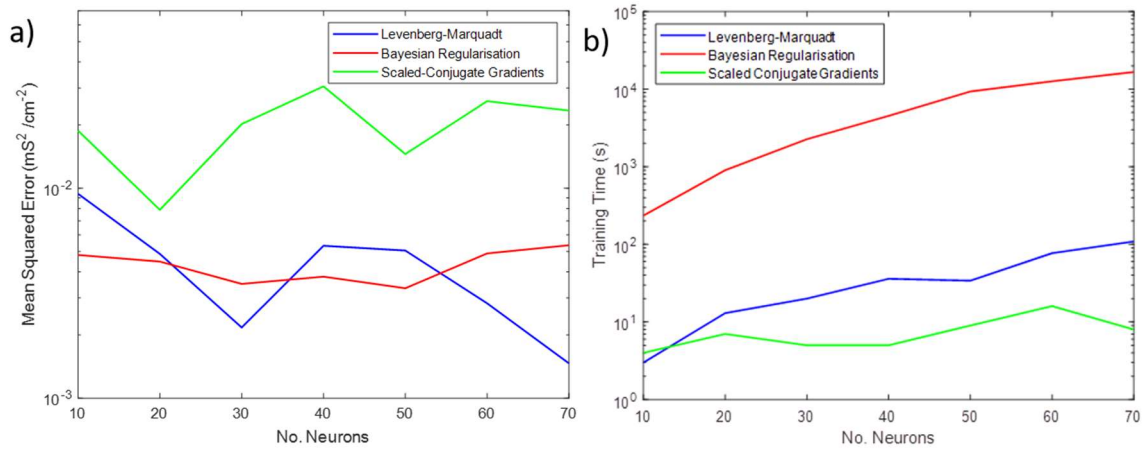

Figure 7 Training algorithm performance: a) algorithm optimisation – MSE; b) training time

On average, the Bayesian Regularisation (BR) training algorithm, yields the smallest test MSE of 0.0043 $mS^2\ cm^{-2}$; however, the average training time required for this algorithm was in excess of 4.5 hours. This ensures that a model capable of being rapidly retrained using new experimental data is unable to be created using a Bayesian approach; this is not preferable. The scaled-conjugate gradient algorithm offers a reduced training time with the lowest accuracy of all of the training algorithms. However, the LM model also remains highly accurate, with the smallest MSE of 0.0015 $mS^2\ cm^{-2}$ observed with an average training time of 100 s, two orders of magnitude smaller than was observed when using BR.

From such an analysis, it is evident that the Levenberg-Marquadt algorithm is the most suitable algorithm for the measurement of aqueous fluid conductivity, based upon the criteria of accuracy and training time. This optimised neural network architecture and training algorithm has been selected and is utilised throughout the remainder of this paper.

A Bayesian Regularisation approach is often suited to noisy training data (Neal, 1996) with the potential of the EIF likely extended to recognise more complex relationships and interactions than explored within this paper. This analysis has enabled the number of hidden layers in the algorithm to be optimised, with thirty neurons in the hidden layer chosen to finalise the architecture.

4.3 Aqueous Phase Conductivity Prediction in 'Dispersed' Flows

Now optimised, the algorithms can be utilised to assess the ability of EIF to predict continuous phase conductivity in multi-phase slurries where solids are present. This analysis was performed across 48,000 fingerprints, which consisted of ninety compositions of slurries which contain kaolin, sand or both. The largest volumetric concentration of solids equated to 28 vol%; this is near to the highest volumetric concentration, of 35 vol %, where EIT densitometry is able to operate. As described in Section 3, 70 % of the data was selected as the training dataset; this consists of 34,300 electrical impedance fingerprints.

Across the entire dataset, the RMSE error in continuous phase conductivity, compared to the conductivity probe data obtained prior to the addition of solids, was found to be 0.055 mS cm^{-1}; this represents an error of less than 1 % of the average conductivity. This level of accuracy is sufficient for the hydraulic conveying application and hence outlines the suitability of EIF to measure in-line conductivity in multi-component slurries. When this is applied to non-nucleonic densitometry, this ensures that accurate density measurements (< ±5 %), are captured across a much extended range of electrical conductivities of 1.5 – 70 mS cm^{-1}.

This performance is highlighted within the parity plot, Figure 8a. From this plot, it is evident that the model can predict the conductivity in a linear manner with a linear regression providing a gradient of 1.001 and a y-intercept of 3.2×10^{-5} mS cm^{-1}. Moreover, the associated correlation coefficient of this linear regression has been found to be 0.9996. This linear comparison approach is justified due to an extremely negative AIC of -41198 with the repeatability of this technique demonstrated by 0.049 % of the entire dataset classified as outliers.

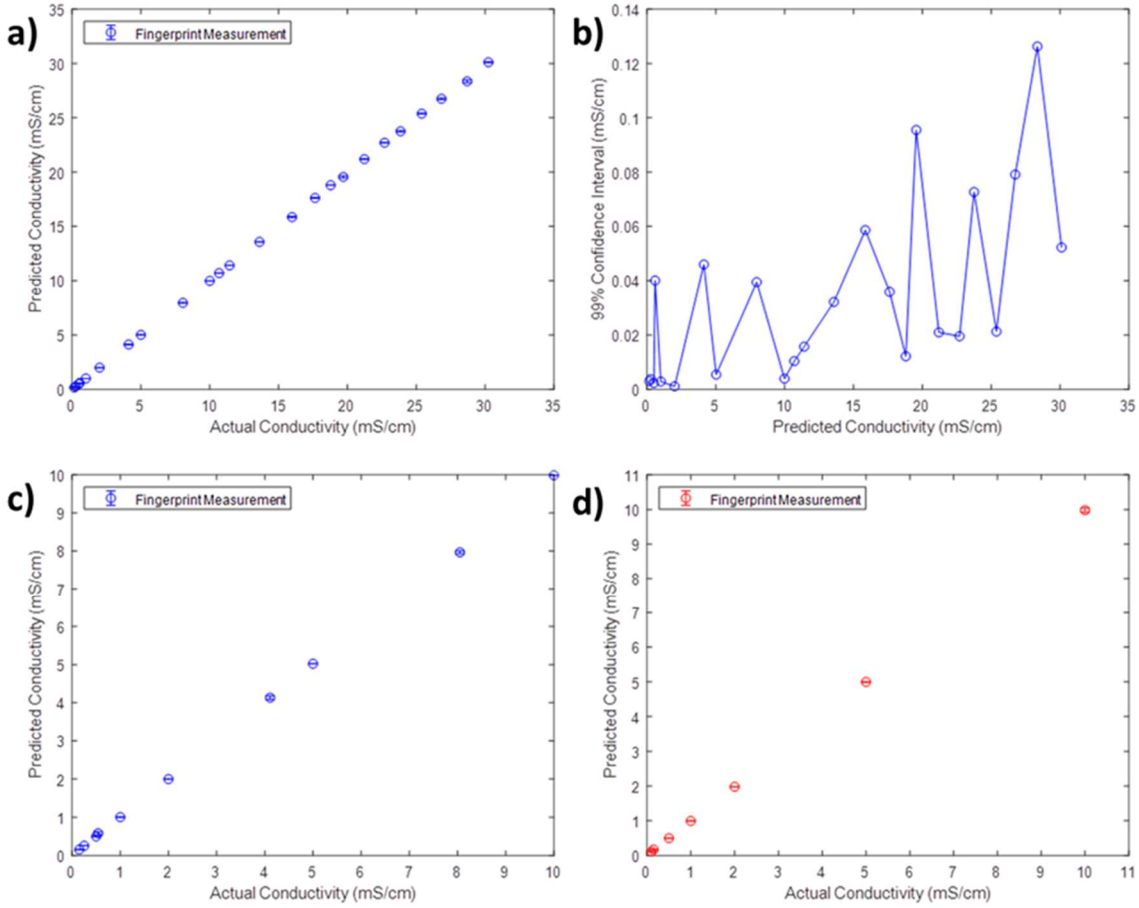

Figure 8 Continuous phase conductivity model: a) parity plot; b) 99 % confidence intervals; c) parity plot when solids are not present; d) parity plot when solids are present

Despite the already high performance, the accuracy of the system can be enhanced further, by developing and training two separate models for the following aqueous conductivity ranges, 0.15 – 10 mS cm^{-1} and greater than 10 mS cm^{-1}. In the range 0.15 – 10 mS cm^{-1}, the RMSE is reduced by 56 % to 0.024 mS cm^{-1}; this represents an average error in the measurement of just 0.54 %. If this model was implemented with the tomographic density measurement, it has the ability to enhance the operable range of aqueous conductivity, to 0.48 – 70 mS cm^{-1}. This range covers the majority of targetted mining and dredging operations. These algorithms may be tailored to the desired process application and operational envelope to enhance their performance and outputs i.e. reservoir dredging, river dredging.

The confidence intervals have also been computed, to assess the uncertainty in the measurement. To do so, it has been assumed that the data is distributed normally. The 99 % confidence intervals are depicted in Figure 8b. From this figure, it has been demonstrated that the maximum CI_{99} was 0.127 mS cm^{-1} which represents just 0.44 % of the measured conductivity, to demonstrate the lack of uncertainty in the measurement.

To demonstrate the independence of EIF to solids in dispersed phase flows, the datasets were segregated into those containing solids and those which did not. The previously derived neural network for the range of 0.15 – 10 mS cm^{-1}, was first applied to fluid systems where no solids were present with a RMSE of 0.026 mS cm^{-1} obtained. Whilst this error is greater than the original model, it represents a minor increase of just 0.002 mS cm^{-1}; this equates to a minor increase of 8.3 %. Such a

minor reduction in performance highlights the suitability of the algorithm to extract continuous phase conductivity irrespective of the presence of solids. This is reflected in the linearity of the parity plots presented in Figures 8c and 8d which represent the predicted aqueous phase with and without solid inclusions, respectively. It must be noted that the same algorithm is employed in both instances.

This demonstrates that the novel technique, EIF, can accurately predict the continuous phase conductivity within multiphase slurries, in-line and in real-time. This technique is performed simultaneously with the EIT density measurement with a high temporal resolution of 0.5 Hz. Upon completion of training, the developed model is capable of making and accurate prediction of continuous phase conductivity at a rate of 28,000 Hz. This high temporal resolution ensures that EIF is able to act as a real-time measurement capable of interrogating dynamic processes. The target operations, require a liquid phase conductivity measurement every 10 – 30 seconds with the robustness of the aqueous phase conductivity able to be further improved with a moving average.

4.4 Robustness to Electrode Failure

A limiting factor of the other non-nuclear technologies which are applied to density measurements, is a lack of robustness to the harsh environment which they are exposed to. This is especially prevalent in dredging operations (Batey, 2012). In some circumstances, the tomography electrodes may become inactive and no longer provide appropriate phase and density information. To mimic this, the phase information associated with the failure of both a single electrode and two adjacent electrodes opposite to the current source injection was removed. These scenarios lead to a reduction in the number of phase measurements which make up the fingerprint from 104 measurements to 78 and 66 for a single and double electrode failures, respectively.

Initially, it was attempted to fit the previously developed model to the new fingerprint, with the inactive measurements values set to 0. As anticipated, this yielded a much-reduced correlation coefficient of 0.39 when the predicted conductivity is compared to the measured conductivity with no predicted value in excess of 22 mS cm^{-1}. Thus, in both instances new networks were trained to generate significant improvements in the predictive behaviour. In the case of a single electrode failure (SEF), performance was analogous to that without electrode failure with a slightly improved RMSE of 0.049 mS cm^{-1} being observed. A minor increase in the maximum CI_{99} was witnessed which was found to increase to 0.134 mS cm^{-1}, 0.46 % of the measured value, to demonstrate low uncertainty within the measurement. The negligible reduction in accuracy with the removal of inputs to the neural network presents an opportunity to further optimise EIF with respect to temporal resolution and computational efficiency. However, it is recommended that all 104 measurements are utilised in the majority of cases as the model is most robust and already considered adaptive.

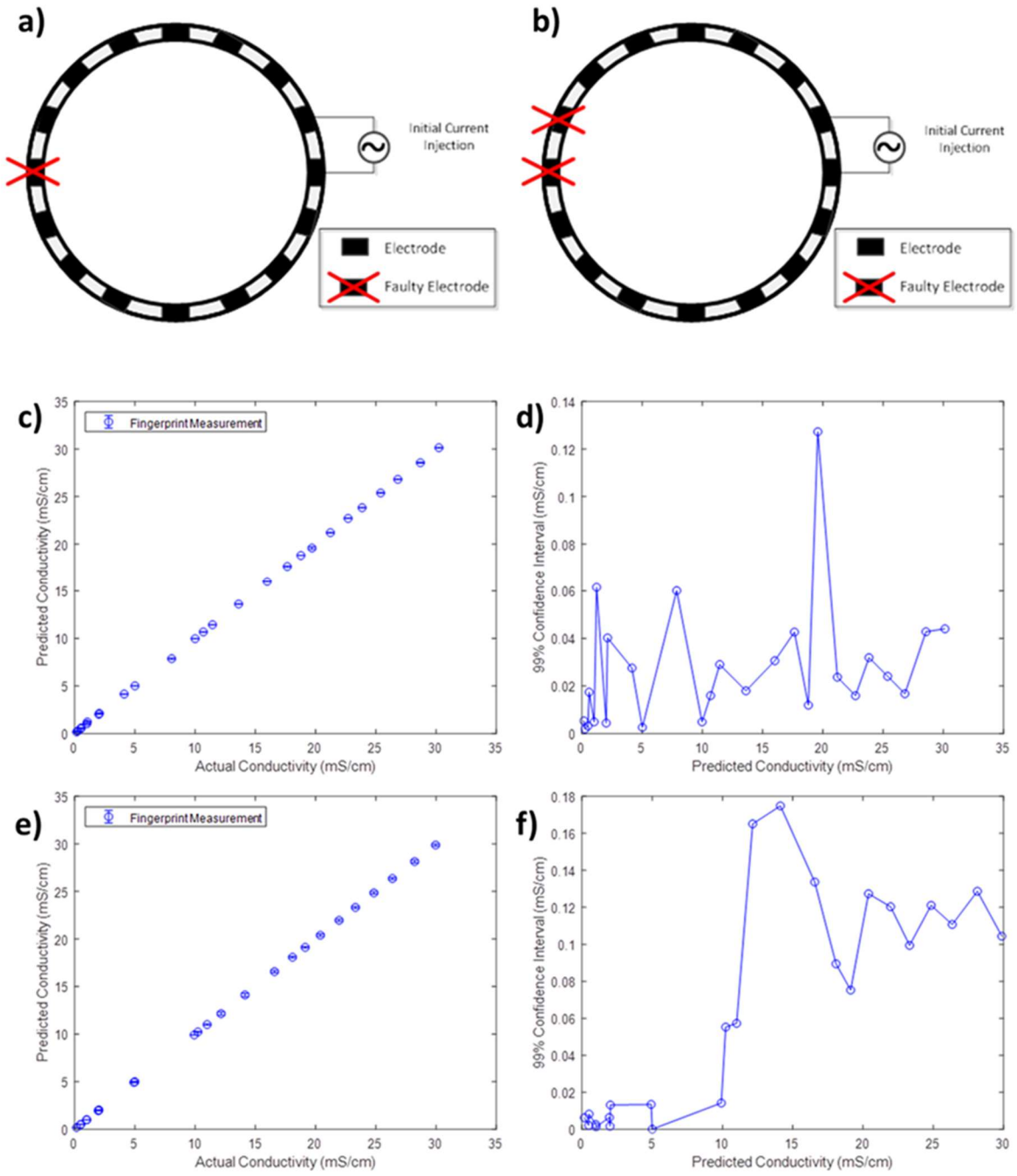

Figure 9 Assessment of EIF during electrode failure: a) single electrode failure (SEF); b) two-adjacent electrode failure (AEF); c) SEF parity plot; d) SEF 99% confidence intervals; e) SEF parity plot; f) SEF 99% confidence intervals

A similar analysis can be repeated when two adjacent electrodes are inactive (AEF) with an increase in RMSE observed to 0.078 mS cm^{-1} and maximum CI_{99} of 0.178 mS cm^{-1}. Despite this increase this algorithm is still capable of accurately and repeatedly capturing the in-line continuous phase conductivity despite the removal of 37 % of the inputted phase information. This behaviour is captured in Figures 9c to 9d and Figures 9e to 9f for a SEF and AEF, respectively. It must additionally be noted that in the latter scenario, if the inactive electrodes are no longer adjacent, the number of measurements will alter ensuring the novel networks are unable to be applied. However, this would also be problematic for the primary EIT applications. This confirms that the EIF technique is not only

promising, but also extremely robust to the harsh conditions exhibited during some hydraulic conveying systems, enhancing the applicability of EIF. It must be acknowledged that this setup would require an electrode self-check system to be implemented to appropriately select the secondary predictive neural networks.

This also demonstrates an additional opportunity for further analysis to reduce the number of phase measurements and amount of training data required to obtain appropriate algorithms, using EIF. A selective reduction in the electrode measurements may lead to an improved temporal resolution and reduction in computational and training requirements of the technology.

4.5 Heterogeneous Flows

Whilst nuclear density meters are often oriented vertically, it is acknowledged that the density measurement may be performed horizontally. In such transport setups an increased number of flow regimes are observed with bed flows likely due to solids deposition (Silva et al, 2016; Lucas et al, 1999). Additional experiments were conducted with the sensor oriented horizontally, with the formation of a solids bed visualised through the transparent EIT sensor. It must be acknowledged that the nature of the bed was not completely characterised.

The presence of a large bed was seen to impact upon the electrical impedance fingerprint with the uniform parabolic phase measurements disturbed. Figures 10a and 10b, represent the Electrical Impedance Fingerprint for a dispersed and bed flows, respectively; the aqueous phase conductivity was fixed at 0.5 mS cm^{-1}.

As the change in Electrical Fingerprint is visible by eye, it is highly likely that such changes may be captured using the artificial intelligence approaches discussed throughout this paper. This presents an opportunity for EIF to extract further critical process information such as the flow regime in multiphase systems i.e. gas-liquid mixing operations. When comparing dispersed and bed flows, the largest change in the electrical impedance fingerprint occurs at electrode measurements located opposite each other in the pipe. These opposite locations relate to measurement numbers 7, 20, 33, 43 and 56 of the fingerprint, as can be seen in Figure 10b. This implies that the fingerprint interrogates the entire cross-section of the pipe, or sensing region, not just the near-wall region.

In hydraulic transport applications, the knowledge of the flow regime would help inform process decisions to maximise pumping efficiency and ensure that a pipeline blockage does not occur. In EIT densitometry, it is also important to identify when a pipe is partially filled; this approach is likely to provide such information to further enhance the capability of EIT operating within hydraulic transport applications.

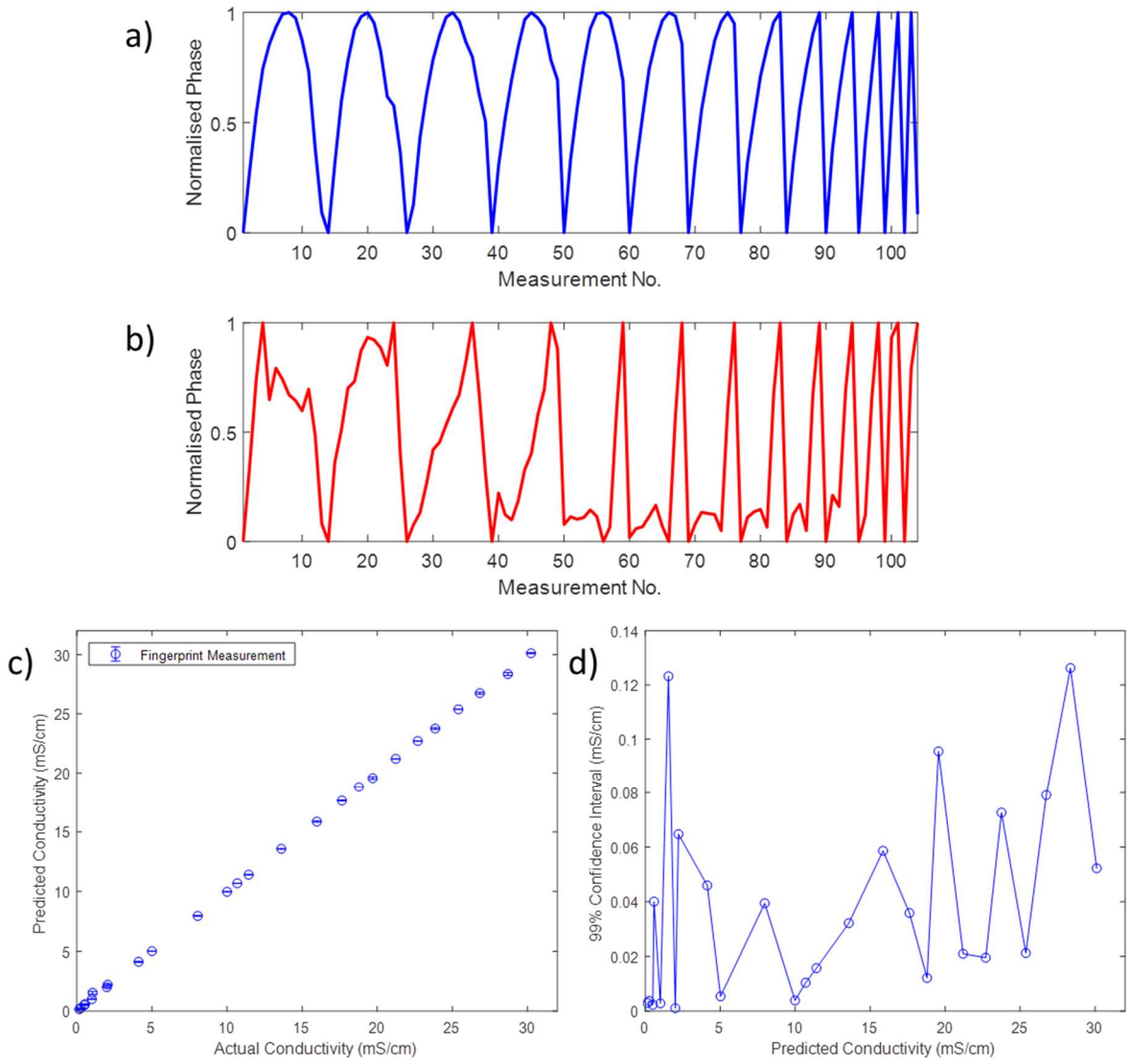

Figure 10 Electrical Impedance Fingerprint in different flow regimes: a) dispersed flow fingerprint – 0.5 mS cm^{-1}; b) horizontal bed flow fingerprint – 0.5 mS cm^{-1}; c) prediction of continuous phase conductivity in bed flow; d) confidence intervals in bed flows

With respect to the measurement of aqueous phase conductivity, the approach outlined in the previous section, Section 4.4, may be extended. In bed flows, the majority of the solid phase exist in a concentrated bed along the bottom of the pipe. Thus, the fingerprint behaviour was investigated with phase measurements located at the top of the pipe; this reduced the number of from 104 to 22 measurements. Using this relatively small amount of phase information, a correlation coefficient of 0.998 is still obtained with a RMSE of 0.158 mS cm^{-1} to demonstrate the applicability of this technique to horizontal bed flows. The performance of this measurements is depicted in Figure 10c. Applying the null hypothesis, the p-values obtained from both parameter estimate, effect testing and variance analysis are below 0.001 indicating a high statistical significance between the predicted and monitored conductivity variables. The amount of data collected in the horizontal orientation was relatively small compared to the vertical installation of the sensor, therefore the datasets were not combined to ensure class imbalance did not occur.

This demonstrates the ability of EIF to monitor the aqueous phase conductivity in both homogeneous and heterogeneous slurry flows. In addition to this, a variation in the fingerprint was visible when the solids were dispersed or when a bed was present. As a result, it is anticipated that EIF is also able to monitor the flow regime present during hydraulic conveying operations, to help optimise pump efficiency and prevent pipeline blockage.

4.6 The Linear Fingerprint

There are two conventional Electrical Tomography sensor arrangements: circular, utilised throughout this study, and linear. Linear arrays, depicted in Figure 11a, have increased flexibility compared to circular arrays as they may be retrospectively retrofitted into existing applications, i.e. a froth flotation tank. Applying EIF principles to linear arrangements improves in-plant applicability of the characterisation technique. Typical pipeline installations employ a circular electrode arrangement; however, the ability to monitor aqueous phase conductivity using linear arrays was also investigated.

As expected, unlike in circular arrays, low admittivity media does not give rise to a uniform parabolic fingerprint for each measurement cycle. Despite this, a repeatable saw-tooth pattern can be observed, with exception of the first measurement cycle, see Figure 11b. According to the 16-electrode linear adjacent-electrode EIT measurement protocol, Figure 11a, the first current injection is performed across electrodes 1 and 16 with the differential voltage measured at the remaining adjacent pairs. The second cycle utilises electrodes 1 and 2 for the current injection with the outputted phase measurements representative of differential voltage measurements with increasing electrode number.

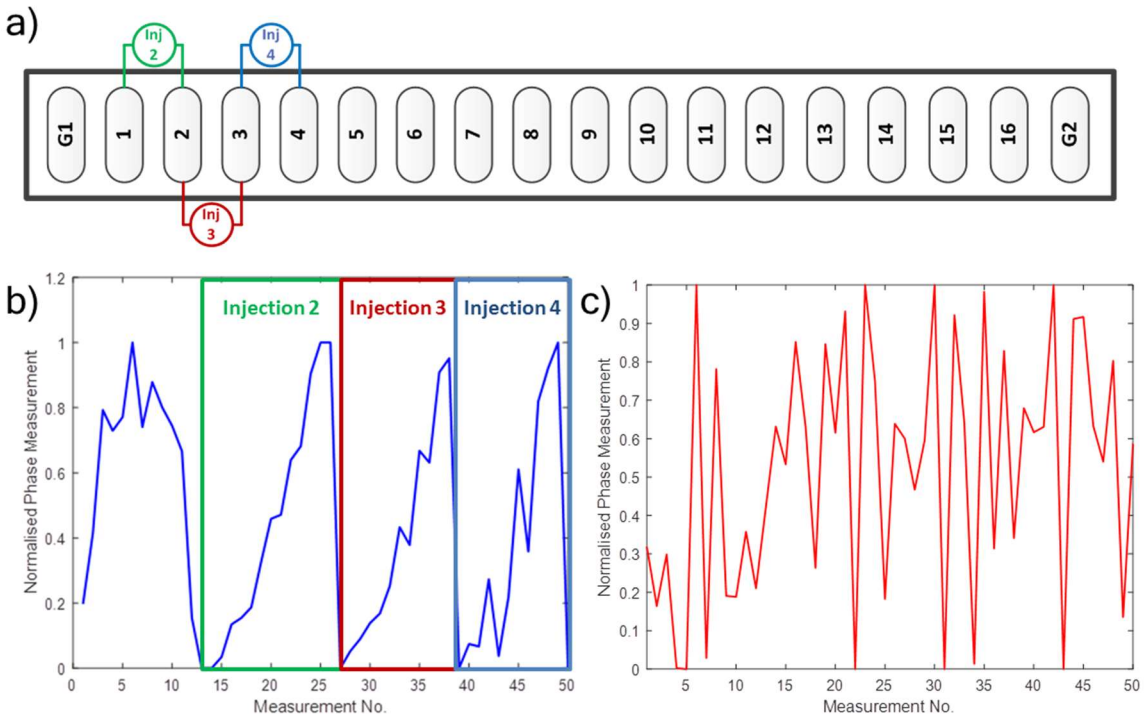

Figure 11 The linear Electrical Impedance Fingerprint: a) linear injection protocol; b) low admittivity media; c) high admittivity media

When the admittivity of the fluid is changed, once again the EIF fingerprint begins to break down into a more disordered structure which has the capability to be identified and related to the key quality parameters of a formulation, Figure 11c.

A 0.3 m linear probe was installed vertically, in an unagitated vessel containing water only whose electrical conductivity was varied between 0.1 – 30 mS cm^{-1}, via the addition of sodium chloride. Despite the electrical impedance fingerprint being saw-tooth in nature, and not uniformly parabolic, the linear array was able to capture the continuous phase conductivity effectively and accurately. The associated RMSE was 0.017 mS cm^{-1}; this represents a minor improvement accuracy compared to the circular arrays. A similar reduction was also observed when analysing the confidence intervals with the maximum confidence interval found to be 0.072 mS cm^{-1}. This performance is reflected in the parity plots depicted in Figure 12a and 12b. The outputs from the EIF approach were also found to be strongly linear with a linear regression with a gradient of 1.002 and y-intercept of -0.0039 yielding a correlation coefficient of 0.9999.

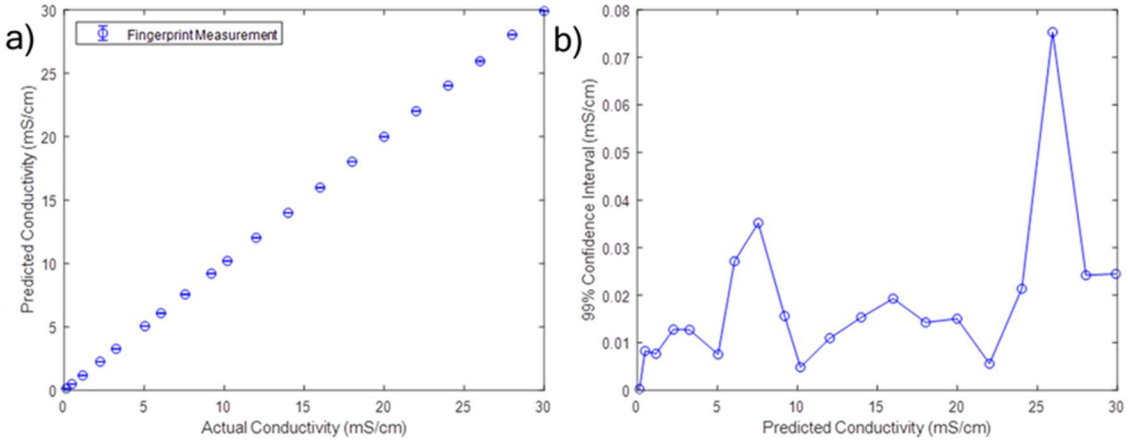

Figure 12 Linear in-line continuous phase conductivity prediction: a) parity plot; b) 99 % confidence interval

This demonstrates that the Electrical Impedance Fingerprinting approach is valid in both circular and linear tomography array types. Linear arrays can be easily retrofitted into process equipment, such as agitated vessels for froth flotation, improving in-plant applicability. Whilst it is not anticipated that this sensing arrangement will be adopted in conventional hydraulic conveying operations, EIF could be utilised to monitor the evolution of formulation properties and structural properties, within a stirred tank, to optimise hydrodynamic conditions, energy consumption and product quality.

5. Conclusions

A novel technique, Electrical Impedance Fingerprinting (EIF) has been presented which utilises phase information obtained from non-invasive micro-electrical tomography sensors to extract the aqueous phase conductivity in multi-component slurries. This conductivity measurement is essential in the operation of a non-nuclear alternative to the density measurement in hydraulic conveying applications, to enhance its accuracy, improve analysis algorithm selection and voltage compensation.

EIF overcomes difficulties in using conductivity probes, which often are unable to measure the aqueous phase without the presence of solids, or be located directly in the sensing region. EIF uses the shape of phase measurements in tomographic sensors to fingerprint the fluid in the pipe. This is

achieved by using artificial intelligence techniques to identify the fingerprint, based upon *a priori* knowledge, which can then be directly related to key process properties, in this study liquid phase conductivity.

To verify the ability of the technology, a number of kaolin/sand slurries were formulated with liquid conductivities in the range of 0.1 – 30 mS cm^{-1}. Upon optimising the neural network architecture, the liquid phase conductivity was accurately predicted with a RMSE of 0.05 mS cm^{-1}, across 50,000 frames of data. This improvement ensures that the non-nuclear density measurement can operate accurately within the aqueous phase conductivity range of 1.48 – 70 mS cm^{-1}; this encompasses the majority of the target minerals engineering applications. A linear regression between the conductivity probe and EIF was also performed and yielded a correlation coefficient of 0.9996.

Due to the harsh environment observed in hydraulic conveying operations, the robustness of EIF to electrode failure has been validated. The response to electrode failure was examined, by reducing the number of measurement points in the fingerprint data. The failure of a single electrode, would reduce the fingerprint from 104 to 66 measurement points. Despite this reduction, the RMSE was seen to reduce to 0.049 mS cm^{-1}. Not only does this demonstrate the robustness of the technology to its target operations, but also presents an opportunity to reduce the number of measurement points and resultantly the computational requirements of the technology.

An analysis was also performed with the sensor oriented horizontally with a solid bed present. In this case, a change in the impedance fingerprint visibly differed to that of dispersed flows. This presents an opportunity for the technique to extend the application of EIF to flow regime detection to inform decisions to optimise pumping efficiency and prevent pipeline blockage. EIF was additionally validated using a linear sensor array type, with results improve compared to circular arrays. Whilst it is not anticipated that this approach will be adopted in hydraulic conveying applications, linear arrays are able to be retrospectively fitted into existing installations, i.e. in froth flotation, increasing in-plant applicability of this technique.

6. Acknowledgements

This work is a part of an EngD project which is financed by the EPSRC Centre for Doctoral Training in Formulation Engineering (EP/L015153/1), Industrial Tomography Systems PLC and the University of Birmingham.

7. References

Ayranci, I; Kresta, S. M. (2014). Critical analysis of Zweitering correlation for solids suspension. *Chemical Engineering Research and Design:* 92 (3), 413-422.

Batey, R.H. (2012) A non-nuclear density meter and mass flow system for dredging slurries. *WEDA XXXII Technical Conference – Conferefence Proceedings: San Antonio, Texas.*

Bennett, M. A; Williams, R. A. (2004). Monitoring the operation of an oil/water separator using impedance tomography. *Minerals Engineering:* 17, 605 – 614.

Bernades, R; Costelo-Branco, M. (2017). Optical coherence tomography – machine learning. *Acta Opthalmologia.*

Chawla, N. V; Lazarevic, A; O'Hall, L; Bowyer, K. (2003). SMOTEBoost: Improving prediction of the minority class in boosting. *Proceedings Principles Knowledge and Discovery: Databases.*

Cullivan, J. C; Williams, R. A; Cross, C. R. (2003). New Insights into hydocyclone operation. *Particulate Science and Technology:* 21, 83 - 103

Cullivan, J. C; Williams, R. A; Dyakowski, T; Cross, C. R. (2004). New understanding of a hydrocyclone flow field and separation mechanism from computational fluid dynamics. *Minerals Engineering:* 17, 605-614.

Dyakowski, T; Jaworsk, A. (2003). Non-Invasive Process Imaging – Principles and Applications of Industrial Process Tomography. *Chemical Engineering Technology: 26 (6), 697, 706.*

Fangary, Y. S; El Ghani, A. S; El Haggar, S. M; Williams, R. A. (1997). The Effect of Fine Particles on Slurry Transport Processes. *Minerals Engineering:* 10, 427-439.

Freund, Y; Schapire, R. (1996). Experiments with a new boosting algorithm. *Proceedings 13th International Conference of Machine Learning, 148 – 155.*

Golgoun, S.M; Sardari, D; Sadeghi, M; Mofrad, F.B. (2016) A novel method of combined detector model for gamma-ray densitometer: Theoretical calculation and MCNP4C simulation. *Applied Radiation and Isotopes:* 118, 246-250.

Gurney, K. (1997). *An Introduction into Neural Networks.* UCL Press: London.

Hartmann, B; King, W. P; Nayarana, S. (2019). *Digital Manufacturing: The Revolution will be Virtualized.* McKinsey & Company: New York.

Hastie, T ; Tibishirani, R ; Friedman, J. (2008). *Eléments of Statistical Learning: Data Mining, Inference and Prediction.* Springer: New York.

Industrial Tomography Systems (2020). P2+ Manual

Industrial Tomography Systems (2020). Z800 Manual

Jiang, Y; Soleimani, M. (2018). Capacitively Coupled Electrical Resistance Tomography (CCERT). *19th Internation Conference on Biomedical Applications of Electrical Impedance Tomography.*

Johansen, R; Østby, T.G; Dupre A; Mylvaganam, S. (2018). Long Short-Term Memory Neural Networks for Flow Regime Identification using ECT. *WCIPT 9: Conf. Proceedings.*

Jones, B; Goos, P. (2011). *Optimal Design of Experiments: A Case Study Approach.* John Wiley and Sons: New York.

Kalender, W. A. (2006). X-ray Computed Tomography. *Physics in Medicine and Biology:* 51, 29 – 43.

Kohn. D. H. (1995). Acoustic Emission and Nondestructive Evaluation of Biomaterials and Tissues. *Critical Reviews in Biomedical Engineering:* 23, 221 – 306.

Lucas, G. P; Cory, J; Waterfall, R. C; Low, W. W; Dickin, F. J. (1999). Measurement of the solids volume fraction and velocity distributions in solids-liquid flows using dual-plane electrical resistance tomography. *Flow Measurement and Instrumentation:* 10, 249 – 248.

Machin, T.D; Wei, H; Greenwood, R.W; Simmons, M.J.H. (2018). In-pipe Rheology and Mixing Characterisation using Electrical Resistance Sensing. *Chemical Engineering Science:* 187, 327-341.

Markel, V. (2016). Introduction to the Maxwell-Garnett Approximation. *Journal of Optical Society of America A:* 1, 1–12.

McCormack, D; Primrose, K; Qiu, C; Wei, K. (2014). Development and Deployment of a Non-Nuclear Densitometer Based on Electrical Resistance Tomography. *21st World Dredging Congress and Exhibition Conference Proceedings.*

Mohammed-Saleh, J; Hoyle, B.S. (2002). Determination of multi-component flow process parameters based on electrical capacitance tomography data using artificial neural networks. *Measurement Science and Technology: 13, 1-7.*

Neal, R. (1996). *Bayesian Learning for Neural Networks.* Springer: New York.

Nowaskowski, A. F; Cullivan, J. C; Williams, R. A; Dyakowski, T. (2004). Application of CFD to modelling the flow of hydrocyclones. Is this a realizable option or still a research challenge?. *Minerals Engineering:* 17, 661 – 669.

Rashid, T. (2016). *Make your own Neural Network.* Elsevier: Amsterdam.

Ru, Y; Pradeep, C; Mylvaganam, S. (2011). Neural Networks in electrical capacitance tomography (ECT) - based detection. *Measurement Science and Technology: 22(10).*

Scott, D. M; McCann, H. (2005). *Process Imaging for Automatic Control.* Taylor and Francis, 359 – 400.

Seiffert, C; Koshggoftaar, T. M. (2010). RUSBoost: A Hybrid Approach to Alleviating Class Imbalance. *IEEE Transactions on Systems, Man and Cybernetics:* 40 (1), 185 – 196.

Silva, R; Faia, P. M; Garcia, F. A. P; Rasteiro, M. G. (2016). Characterization of solid-liquid settling suspensions using Electrical Impedance Tomography: A comparison between numerical experimental and visual information. *Chemical Engineering Research and Design:* 111, 223 – 242.

Soleimani, M; Lionheart, W. (2005). Nonlinear Image Reconstruction for Electrical Capacitance Tomography using Experimental Data. *Measurement Science and Technology:* 16 (10), 1987 - 1996

Stephenson, D. R. (2008). *Choices and Implications in Three-Dimensional Electrical Impedance Tomography.* EngD Thesis, University of Manchester.

Tan, C; Xu, Y ; Dong, F. (2011). Determining the boundary conditions of inclusions of known conductivities using a Levenberg-Marquadt algorithm by Electrical Resistance Tomography. *Measurement Science and Technology:* 22.

Wang, M; Jones, T. F; Williams, R. A. (2003). Visualization of asymmetric solids distribution in horizontal swirling flows using electrical resistance tomography. *Trans IChemE:* 81A, 854-861

Wang, M. (2015). Industrial Tomography: Elsevier Science, Amsterdam.

Wei, K; Qiu, C; McCormack, D; Primrose, K. (2016). ITS Dens-Itometer: An Electrical Resistance Tomography Based Densitometer. *WCIPT 8: Conference Proceedings, Brazil.*

Williams, R. A; Beck, M. S. (1995) *Process Tomography: Principles, Techniques and Applications.* Elsevier Science and Technology, Amsterdam.

Williams, R. A; Jia, X; West, R. M; Wang, M; Cullivan, J. C; Bond, J; Faulks, I; Dyakowski, D; Wang, S. J; Climpson, N; Kostuch, J. A; Payton, D. (1999). Industrial Monitoring of Hydrocyclone Operation using Electrical Resistance Tomography. *Minerals Engineering:* 12, 1245-1252.

Williams, R. A; Vilar, G. (2008). Measurement of suspension velocity in slurries and pastes using impedance imaging. *Journal of Southern African Institute of Mining and Metallurgy:* 106, 1-9.

Wright, J; Colling, A. (1995). *Seawater: Its Composition, Properties and Behaviour.* Elsevier Science: Burlington.

York, T. (2001). Status of Electrical Tomography in Industrial Applications. *Journal of Electronic Imaging:* 10 (3), 608–619.

Zimnyakov, D. A; Tuchin, W. (2002). Optical Tomography of Tissues. *Quantum Electronics:* 32, 849 – 867.